Backscattered energetic neutral atoms from the Moon in the Earth's plasma sheet observed by Chandarayaan-1/Sub-keV Atom Reflecting Analyzer instrument

AUTHOR(S):

Harada, Yuki; Futaana, Yoshifumi; Barabash, Stas; Wieser, Martin; Wurz, Peter; Bhardwaj, Anil; Asamura, Kazushi; ... Yokota, Shoichiro; Tsunakawa, Hideo; Machida, Shinobu

CITATION:

Harada, Yuki ...[et al]. Backscattered energetic neutral atoms from the Moon in the Earth's plasma sheet observed by Chandarayaan-1/Sub-keV Atom Reflecting Analyzer instrument. Journal of Geophysical Research: Space Physics 2014, 119(5): 3573-3584

ISSUE DATE:

2014-05-20

URL:

http://hdl.handle.net/2433/198618

AGU PUBLICATIONS

JGR

Journal of Geophysical Research: Space Physics

RESEARCH ARTICLE
10.1002/2013JA019682

Key Points:
- We present ENA observations at the Moon in the Earth's plasma sheet
- Plasma sheet protons are backscattered as ENAs from the lunar surface
- Magnetic shielding in the plasma sheet is less effective than in the solar wind

Correspondence to:
Y. Harada,
haraday@kugi.kyoto-u.ac.jp

Citation:
Harada, Y., et al. (2014), Backscattered energetic neutral atoms from the Moon in the Earth's plasma sheet observed by Chandarayaan-1/Sub-keV Atom Reflecting Analyzer instrument, *J. Geophys. Res. Space Physics*, *119*, 3573–3584, doi:10.1002/2013JA019682.

Received 2 DEC 2013
Accepted 27 APR 2014
Accepted article online 2 MAY 2014
Published online 20 MAY 2014

Backscattered energetic neutral atoms from the Moon in the Earth's plasma sheet observed by Chandarayaan-1/Sub-keV Atom Reflecting Analyzer instrument

Yuki Harada[1], Yoshifumi Futaana[2], Stas Barabash[2], Martin Wieser[2], Peter Wurz[3], Anil Bhardwaj[4], Kazushi Asamura[5], Yoshifumi Saito[5], Shoichiro Yokota[5], Hideo Tsunakawa[6], and Shinobu Machida[7]

[1]Department of Geophysics, Kyoto University, Kyoto, Japan, [2]Swedish Institute of Space Physics, Kiruna, Sweden, [3]Physics Institute, University of Bern, Bern, Switzerland, [4]Space Physics Laboratory, Vikram Sarabhai Space Center, Thiruvananthapuram, India, [5]Institute of Space and Astronautical Science, Japan Aerospace Exploration Agency, Sagamihara, Japan, [6]Department of Earth and Planetary Sciences, Tokyo Institute of Technology, Tokyo, Japan, [7]Solar-Terrestrial Environment Laboratory, Nagoya University, Nagoya, Japan

Abstract We present the observations of energetic neutral atoms (ENAs) produced at the lunar surface in the Earth's magnetotail. When the Moon was located in the terrestrial plasma sheet, Chandrayaan-1 Energetic Neutrals Analyzer (CENA) detected hydrogen ENAs from the Moon. Analysis of the data from CENA together with the Solar Wind Monitor (SWIM) onboard Chandrayaan-1 reveals the characteristic energy of the observed ENA energy spectrum (the *e*-folding energy of the distribution function) ~100 eV and the ENA backscattering ratio (defined as the ratio of upward ENA flux to downward proton flux) < ~0.1. These characteristics are similar to those of the backscattered ENAs in the solar wind, suggesting that CENA detected plasma sheet particles backscattered as ENAs from the lunar surface. The observed ENA backscattering ratio in the plasma sheet exhibits no significant difference in the Southern Hemisphere, where a large and strong magnetized region exists, compared with that in the Northern Hemisphere. This is contrary to the CENA observations in the solar wind, when the backscattering ratio drops by ~50% in the Southern Hemisphere. Our analysis and test particle simulations suggest that magnetic shielding of the lunar surface in the plasma sheet is less effective than in the solar wind due to the broad velocity distributions of the plasma sheet protons.

1. Introduction

The surface of the Moon is directly exposed to its surrounding plasma due to the absence of both a thick atmosphere and an intrinsic magnetic field. While it has been thought that impinging charged particles are almost completely absorbed in the surface material, recent observations from Kaguya, Chandrayaan-1, and Interstellar Boundary Explorer (IBEX) indicate that ~0.1–1% of the incident solar wind protons are scattered back as ions and ~10–20% as energetic neutral atoms (ENAs) [*Saito et al.*, 2008a; *McComas et al.*, 2009; *Wieser et al.*, 2009]. The observed energy spectra of the backscattered hydrogen atoms are relatively flat up to hundreds of electronvolts and decrease sharply at higher energies [*Rodríguez et al.*, 2012; *Futaana et al.*, 2012; *Funsten et al.*, 2013; *Allegrini et al.*, 2013]. Angular distributions of the backscattered ENAs are almost isotropic for normal incidence of the solar wind, and exhibit anisotropy for large solar zenith angles [*Schaufelberger et al.*, 2011]. *Allegrini et al.* [2013] compared the ENA energy spectra obtained by IBEX when the Moon was located in the magnetosheath with those in the solar wind, showing that the backscattered ENA intensities are generally higher in the magnetosheath. They suggested that a lower Mach number in the magnetosheath increases the surface area of lunar grains illuminated by the incident protons and visible from IBEX.

The Moon does not have a global dipole field, but remanent crustal magnetization is widely but nonuniformly distributed over the lunar surface [*Richmond and Hood*, 2008]. These crustal magnetic fields have a significant impact on the near-lunar plasma environment. *Lin et al.* [1998] suggested the formation of a "minimagnetosphere" as a result of solar wind interaction with lunar magnetic anomalies. Upward ions with extremely large flux up to more than 10% of the solar wind proton flux are observed above magnetic anomalies [*Saito et al.*, 2010; *Lue et al.*, 2011]. Several spacecraft and surface observations as well as

numerical simulations indicate that solar wind protons are reflected or deflected above the surface not only by crustal magnetic fields but also by charge separation electric fields and magnetic fields associated with current systems around magnetic anomalies [*Neugebauer et al.*, 1972; *Clay et al.*, 1975; *Harnett and Winglee*, 2002; *Lue et al.*, 2011; *Bamford et al.*, 2012; *Kallio et al.*, 2012; *Saito et al.*, 2012; *Poppe et al.*, 2012; *Futaana et al.*, 2013]. The solar wind interaction with magnetic anomalies is characterized by the upstream solar wind parameters such as the solar wind dynamic pressure, Mach numbers, strength, and polarity of the interplanetary magnetic field [*Dyal et al.*, 1972; *Harnett and Winglee*, 2000; *Kurata et al.*, 2005; *Halekas et al.*, 2006; *Nishino et al.*, 2012; *Vorburger et al.*, 2012].

An important consequence of the formation of the minimagnetosphere is that the lunar surface might be shielded from the impinging ions. Several authors pointed out correlations between the magnetic anomalies and high-albedo markings on the lunar surface (the lunar "swirls"), and it is proposed that swirl origins are related to differential space weathering due to shielding from the solar wind protons and/or charged-dust transport by electric fields associated with the minimagnetosphere [*Hood and Williams*, 1989; *Hood et al.*, 2001; *Richmond et al.*, 2003; *Richmond and Hood*, 2008; *Garrick-Bethell et al.*, 2011; *Blewett et al.*, 2011; *Hemingway and Garrick-Bethell*, 2012; *Wang et al.*, 2012]. Information about surface distributions of precipitating ion flux is essential for the understanding of the ion shielding processes and their relations with the lunar swirls. However, only a few measurements on the lunar surface of the solar wind ions exist [*Schubert and Lichtenstein*, 1974, and references therein].

Futaana et al. [2006] proposed that lunar ENA observations can be used as a remote sensing technique to estimate the precipitating ion flux onto the surface, and consequently, to image the minimagnetosphere. If a local region on the lunar surface is completely shielded from the incident ions by the magnetic field, no ENAs caused by ion precipitation will be emitted from that region. In fact, a reduction in the ENA flux was observed by CENA above magnetic anomalies, indicating locally effective ion shielding [*Wieser et al.*, 2010; *Vorburger et al.*, 2012]. The CENA observations also revealed an enhanced-flux region surrounding the void region, suggesting increased solar wind flux due to the deflection around the minimagnetosphere. Recently, global ENA maps were produced from the CENA data, which show large reductions in ENA backscattering ratio (defined as the ratio of the upward ENA flux to the downward flux of the upstream solar wind protons) as much as ~50% in large and strong anomaly regions [*Vorburger et al.*, 2013]. In addition, the lunar ENA observations were used to infer a potential difference between the upstream plasma and the lunar surface, which is potentially associated with charge separation above the magnetic anomalies [*Futaana et al.*, 2013].

All of the reported lunar ENA investigations used observations when the Moon was located in the solar wind or magnetosheath. The Moon enters the terrestrial magnetotail for several days around full moon. In the magnetotail, the lunar surface is sometimes exposed to hot plasma of the terrestrial plasma sheet [*Rich et al.*, 1973; *Harada et al.*, 2010, 2012; *Harnett et al.*, 2013]. Plasma parameters in the plasma sheet such as densities, ion and electron temperatures, and Mach numbers significantly differ from those in both the solar wind and magnetosheath. Therefore, lunar ENA characteristics in the Earth's plasma sheet can be quite different from those in the solar wind and magnetosheath. The similarity and difference are directly associated with nature of the interaction between plasma and the regolith surface in space. Here we present ENA, plasma, and magnetic-field data obtained from Chandrayaan-1 and Kaguya when the Moon was located in the Earth's magnetotail and discuss the lunar ENA characteristics in the plasma sheet.

2. Instrumentation and Data Sets

We analyze the data obtained by the Sub-keV Atom Reflecting Analyzer (SARA) instrument onboard Chandrayaan-1, which consists of two sensors: the Solar Wind Monitor (SWIM) and the Chandrayaan-1 Energetic Neutrals Analyzer (CENA) [*Barabash et al.*, 2009]. SWIM measures ions in the energy range from ~100 eV/q to 3 keV/q with mass resolution within a ~ 7° × 160° field of view divided into 16 angular sectors [*McCann et al.*, 2007]. CENA measures energetic neutral atoms (~10 eV to 3 keV) with mass resolution within a 9° × 160° field of view divided into 7 angular sectors [*Kazama et al.*, 2007]. In this paper, we use the CENA data in the energy range of 38–652 eV (energy setting 2) in the hydrogen channels from three angular sectors centered at the nadir-looking direction (sectors 2–4).

Some of the CENA data are contaminated by ultraviolet light, and sometimes, it is difficult to extract the rather weak ENA signal in the magnetotail. Note that signal in the magnetotail is weaker by 2–3 orders of magnitude compared with that in the solar wind. Due to the difficulty, here we only use the CENA data

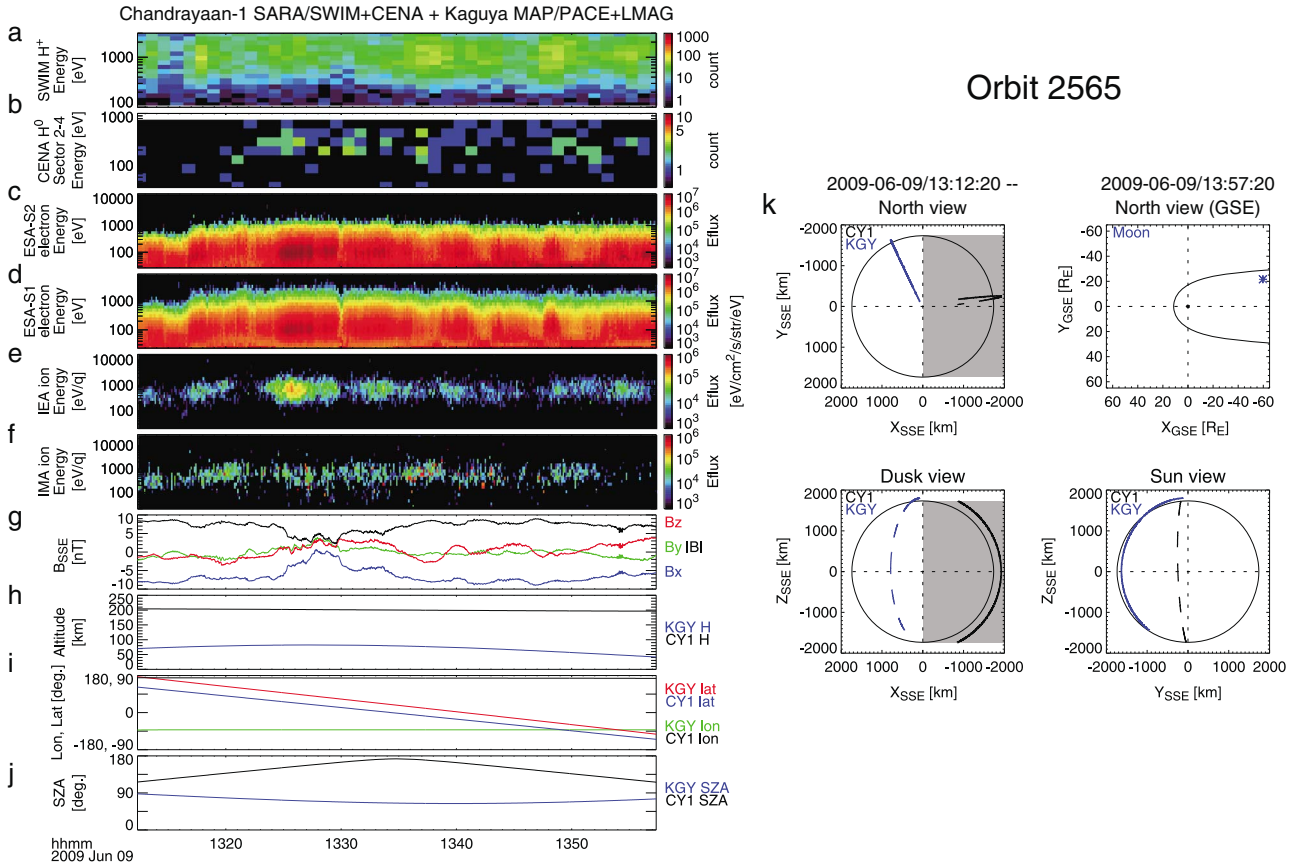

Figure 1. Time series data from Chandrayaan-1 (CY-1; orbit 2565) and Kaguya (KGY) in the terrestrial plasma sheet. Energy-time spectrograms of (a) protons from CY-1/SWIM (64 s data accumulation), (b) hydrogen atoms from CY-1/CENA (64 s data accumulation), (c) downward electrons from KGY/ESA-S1, (d) upward electrons from KGY/ESA-S2, (e) downward ions from KGY/IEA, (f) upward ions from KGY/IMA, (g) magnetic field in SSE coordinates from KGY/LMAG, spacecraft (h) altitudes, (i) selenographic longitudes and latitudes, and (j) solar zenith angles are shown. (k) Chandrayaan-1 and Kaguya orbits in SSE coordinates and the position of the Moon in GSE coordinates (R_E = 6378 km, the gray zones in the left column represent the optical shadow of the Moon and the black line in the top right shows the typical location of the magnetopause).

obtained when the Chandrayaan-1 was in the optical shadow of the Moon. Nevertheless, plasma sheet ions can even precipitate onto the nightside lunar surface. This is because both earthward (corresponding to the sunward motion) and tailward (antisunward) plasma flows exist at the lunar distance ($\sim 60R_E$, where R_E is the Earth's radius of 6378 km) in the Earth's magnetotail [*Mukai et al.*, 1998; *Saito et al.*, 2013]. Moreover, hot protons with nearly isotopic velocity distributions are frequently observed in the central plasma sheet [e.g., *Machida et al.*, 1994]. The nightside lunar surface is exposed to incident protons when the Moon is immersed in the isotropic plasma.

We also present the plasma and magnetic-field data from the MAP (Magnetic field and Plasma experiment) instrument onboard Kaguya to confirm the ambient plasma conditions around the Moon. MAP consists of two components: LMAG (Lunar Magnetometer) and PACE (Plasma energy Angle and Composition Experiment). LMAG measures the magnetic field with a resolution of 0.1 nT [*Shimizu et al.*, 2008; *Takahashi et al.*, 2009; *Tsunakawa et al.*, 2010]. PACE consists of four sensors: two electron spectrum analyzers (ESA-S1 and ESA-S2), an ion mass analyzer (IMA), and an ion energy analyzer (IEA) [*Saito et al.*, 2008b, 2010]. Each sensor has a hemispherical field of view to obtain three-dimensional velocity distribution functions of electrons and ions.

3. ENAs From the Moon in the Earth's Magnetotail

3.1. Overview of Lunar ENA Observations in the Geotail

We first present time series data of ENAs and ambient plasma conditions. Figures 1 and 2 show the SARA data obtained when the Chandrayaan-1 spacecraft was located in the optical shadow of the Moon for orbits

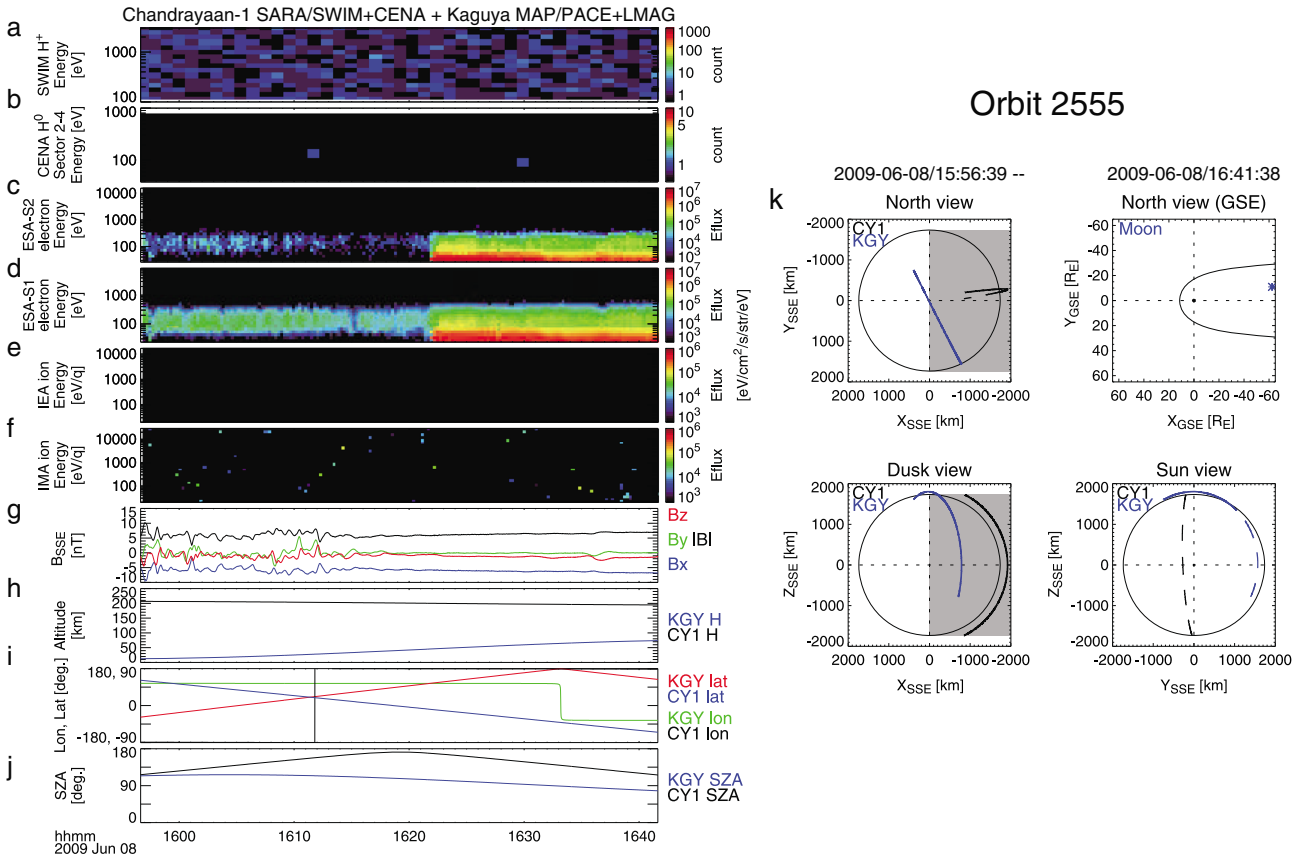

Figure 2. Time series data from Chandrayaan-1 (orbit 2555) and Kaguya in the terrestrial magnetotail lobe in the same format as in Figure 1. Kaguya was illuminated by sunlight after 16:22 UT and intense spacecraft photoelectrons which were attracted by the positive spacecraft potential can be seen in the low-energy part of the (d) ESA-S1 and (c) ESA-S2 data. The fluctuations observed by (g) LMAG at 15:56–16:18 UT at low altitudes are presumably due to lunar crustal magnetic fields.

2565 and 2555, respectively, as well as the plasma and magnetic-field data simultaneously obtained by MAP onboard Kaguya. The selenocentric solar ecliptic (SSE) system has its *x* axis from the Moon toward the Sun, the *z* axis is parallel to the upward normal to the Earth's ecliptic plane, and the *y* completes the orthogonal coordinate set, whereas the geocentric solar ecliptic (GSE) system has its *x* axis from the Earth toward the Sun. The Moon was located in the dawnside magnetotail (~01–02 LT). In orbit 2565, Chandrayaan-1 traveled from north to south ~200 km above the lunar surface at selenographic longitudes of ~ 170°E, while Kaguya was at <100 km altitudes on the near-terminator orbit (Figures 1h, 1i, and 1k). The Chandrayaan-1 orbit track and surface area seen by the CENA angular sectors 2–4 are shown in Figure 3. The projected area in the Southern Hemisphere corresponds to the large magnetic anomaly region, where the ENA backscattering ratio map previously obtained from the CENA data in the solar wind exhibits a significant reduction in ENA backscattering ratio, with reductions up to ~50% [*Vorburger et al.*, 2013]. Kaguya observed hot electrons (Figures 1c and 1d) and ions (Figures 1e and 1f) with energies of hundreds eV up to a few keV, indicating that the Moon entered the terrestrial plasma sheet. The SWIM data also exhibit consistent signatures of hot protons (Figure 1a), which truly show that the Moon was exposed to nearly isotropic flux of the plasma sheet protons. On the other hand, the plasma data from orbit 2555 (Figures 2a and 2c–2f) show the absence of the hot plasma, indicating that the Moon was located in the tail lobe.

Simultaneously, when SWIM identified the plasma sheet protons, CENA detected ENAs from the Moon. Figures 1b and 2b show the energy-time spectrograms of hydrogen ENAs. We see the CENA counts during most of the time of orbit 2565. These continuous signals are not seen in Figure 2b, which only shows very small instrument background counts in the optical shadow. The correlation of the CENA counts with the proton flux detected by SWIM implies that the detected CENA counts are not due to background noise.

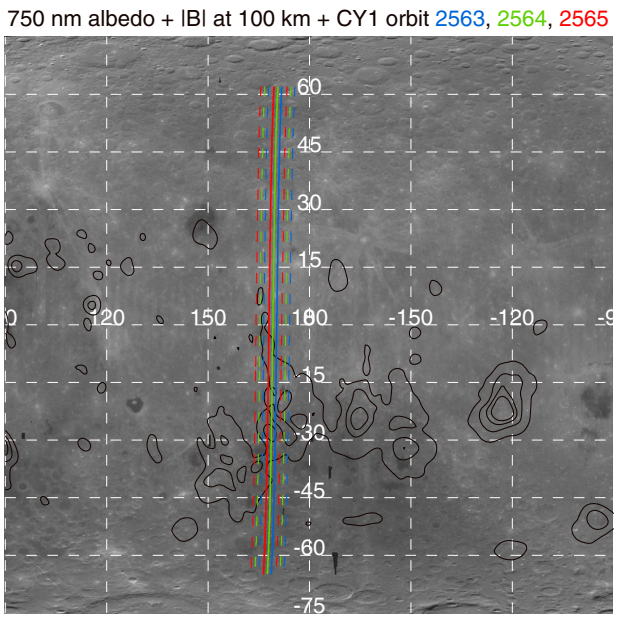

Figure 3. Chandrayaan-1 trajectories in the optical shadow of the Moon during the orbits 2563 (blue), 2564 (green), and 2565 (red). The dashed color lines represent the surface projections of the field of view of the CENA sectors 2–4. The black contours indicate the lunar crustal magnetic field strength at 100 km altitude obtained from Kaguya data with lines for 0.5 nT, 1 nT, 1.5 nT, and 2 nT [*Tsunakawa et al.*, 2010, 2014]. The background grayscale image shows the Clementine 750 nm albedo map.

3.2. ENA Energy Spectrum

ENA energy spectra can constrain generation mechanisms of the ENAs from the Moon in general. Figure 4 shows the energy spectrum of hydrogen ENAs observed by CENA in the optical shadow of the Moon, integrated from orbits 2563 (08:57:12–09:42:12 UT), 2564 (11:04:46–11:49:46 UT), and 2565 (13:12:20–13:57:20 UT) on 9 June 2009. The integration time for each orbit is ~45 min, resulting in a total integration time of ~135 min. During most of the time periods, the Moon was located in the plasma sheet and SWIM observed significant proton flux. The energy spectrum observed in the plasma sheet has a similar shape to the energy spectra of backscattered hydrogen atoms observed by IBEX and Chandrayaan-1 in the solar wind [*Rodríguez et al.*, 2012; *Futaana et al.*, 2012]. *Futaana et al.* [2012] showed that the ENA energy spectra observed by CENA are well reproduced by the Maxwell distribution with typical characteristic energies of ~60–140 eV. The solid curve in Figure 4 shows the fitted Maxwell distribution (the observed data are weighted by the uncertainty due to counting statistics when fitting). The observed spectrum is well fitted by the Maxwell distribution especially in the higher energy range with sufficient statistics. The best fit parameters are the number density $N \sim 0.03$ cm^{-3} and the characteristic energy $kT \sim 100$ eV. The characteristic energy (the best fit temperature, corresponding to the *e*-folding energy of the distribution function) of ENAs in the plasma sheet is very similar to those in the solar wind. As discussed by *Futaana et al.* [2012], the shape of these energy spectra is not compatible with the energy spectra for ion sputtering but can be explained by scattering of ions from the surface of regolith grains, typically involving a few scatter events for a backscattered ENA. Thus, it is most likely that the detected ENAs emitted from the lunar surface while the Moon is in the plasma sheet are also backscattered hydrogen ENAs.

As in *Futaana et al.* [2012], we use the Maxwellian only because it best fits the observed ENA energy spectra. However, this is just an empirically found function and not derived from the physics of multiple-scattering events at the surface. Also, note that the collisionless ENAs in the vicinity of the Moon are not in thermal equilibrium. Therefore, the best fit parameters derived here do not represent the density and temperature of a thermal gas. Physical explanation and detailed discussion of the backscattering processes at the lunar surface are beyond the scope of this paper.

3.3. Backscattering Ratio

Here we investigate the flux ratio of the backscattered hydrogen ENAs to the incident protons. We define the backscattering ratio as

$$r = \frac{F_{xH^0}}{F_{xH^+}} = \frac{\left| \int\int \cos\theta J_{H^0}(E,\Omega)\mathrm{d}E\mathrm{d}\Omega \right|}{\left| \int\int \cos\theta J_{H^+}(E,\Omega)\mathrm{d}E\mathrm{d}\Omega \right|}, \quad (1)$$

where F_{xH^0} is the upward flux of the hydrogen ENAs from the surface, F_{xH^+} is the downward flux of the incident protons onto the surface, θ is the angle between the particle velocity and the surface normal, and J_{H^0}

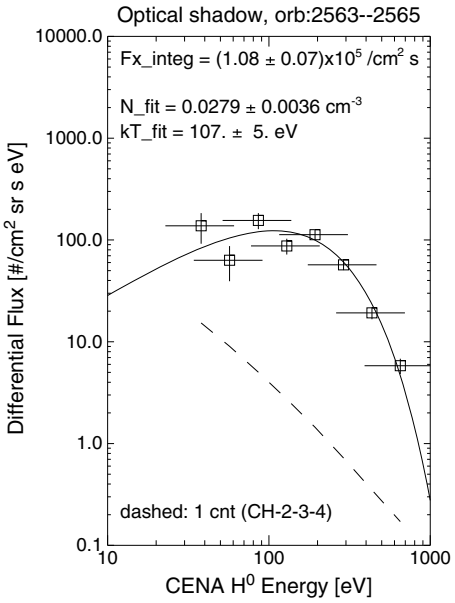

Figure 4. Energy spectrum of upward traveling hydrogen ENAs detected by CENA in the optical shadow of the Moon integrated over the orbits 2563–2565. Error bars correspond to the energy resolution (*x* axis) and the uncertainty due to counting statistics (*y* axis). The upward flux derived from the observed differential flux integrated over the measured energy range is shown with errors from propagation of counting statistics. The solid curve shows the best fitted Maxwell distribution. The fitting parameters with errors from propagation of the fitting errors are also denoted. The dashed line represents the one count level (over 135 min).

and J_{H^+} are the differential number fluxes of the upward hydrogen ENAs and downward protons, respectively. We assume an isotropic angular distribution of the hydrogen ENAs emitted over 2π str from the lunar surface for simplicity as was done in *Futaana et al.* [2012]. The actual angular distribution is not too different from the isotropic one [*Vorburger et al.*, 2013]. Here we derive the hydrogen ENA flux by directly integrating the observed differential flux over the measured energy range. The upward flux of hydrogen ENAs calculated from the data is shown in Figure 4. The flux errors are from propagation of the uncertainty owing to counting statistics.

We analyze the data from SWIM to calculate the downward proton flux impinging the lunar surface. We first conduct spacecraft potential correction. Spacecraft surfaces are charged negatively in the optical shadow due to the larger flux of faster electrons than slower ions [*Whipple*, 1981]. The ambient protons are accelerated by the negative spacecraft potentials before detected by SWIM, resulting in a shift in the energy spectrum toward higher energies. The Chandrayaan-1 spacecraft potential was not directly measured, but we can constrain the upper and lower spacecraft potentials to be between 0 and −250 V, since the lower energy cutoff of the observed proton counts was around 250 eV during orbits 2563–2565. Figure 5 shows the proton energy spectra derived from the SWIM observation with corrections of assumed spacecraft potentials of 0, −150, and −250 V. The energy spectra fitted by the Maxwell distribution and the best fit parameters (the proton density and temperature) are also displayed for reference.

Under the assumption of an isotropic proton distribution just above the Debye sheath formed on the charged lunar surface, the downward proton flux is calculated in the same way as calculation of the upward ENA flux integrating the observed energy spectrum. Since the Debye length (<1 km) is much smaller than the lunar radius (1738 km), acceleration by the negative lunar surface potential will not modify the downward proton flux onto the lunar surface [*Whipple*, 1981]. The downward proton fluxes calculated from the data are shown in Figure 5. Using these fluxes, we obtain backscattering ratios for the measured energy ranges $r \sim 0.051 \pm 0.003$, 0.064 ± 0.004, and 0.076 ± 0.005 for the assumed spacecraft potentials of 0 V, −150 V, and −250 V, respectively. The errors are from propagation of counting statistics of the CENA and SWIM data. These backscattering ratios are comparable to but slightly smaller than the solar wind backscattering ratio of ∼0.1–0.2.

We now investigate the ENA backscattering ratios as functions of selenographic latitude using the downward proton fluxes and upward ENA fluxes derived from the SWIM and CENA measurements. During orbits 2563–2565, Chandrayaan-1 traveled at longitudes ∼ 170°E, where a large magnetized region exists in the Southern Hemisphere (Figure 3). Figure 6 shows backscattering ratios calculated from the data obtained in four different latitude ranges. Previous analysis of the CENA data obtained in the solar wind shows a significant reduction in backscattering ratio up to ∼50% at the same longitude in the Southern Hemisphere at location of strong magnetization of the lunar surface [*Vorburger et al.*, 2013]. The decrease in backscattering ratio can be attributed to the shielding effect of the lunar surface from the solar wind protons above the magnetic anomalies. On the other hand, we note that the north-south asymmetry in the backscattering ratios is less clear in the plasma sheet. Though we see a tendency of smaller backscattering ratio in the Southern Hemisphere, the backscattering ratio difference between the north and south latitudes is at most ∼20%, which is much smaller than ∼50% decrease seen between −30° and −60° latitudes in the solar

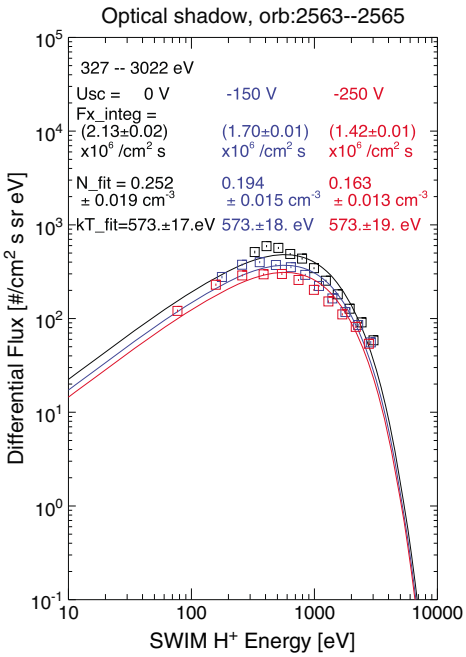

Figure 5. Energy spectra of downward traveling protons obtained by SWIM in the optical shadow of the Moon during orbits 2563–2565 for three cases of assumed spacecraft potentials of 0, −150, and −250 V. The energy spectra are shifted in units of distribution function and converted to differential flux. The denoted downward flux is calculated directly from the data. The shifted energy spectra are fitted by Maxwell distributions, and the solid curves show the fitted distribution.

wind [*Vorburger et al.*, 2013]. The smaller north-south asymmetry in the backscattering ratios suggests less effective magnetic shielding of the lunar surface from the plasma sheet protons than the solar wind protons.

Here we briefly discuss a possible effect of a nonisotropic proton flux in the plasma sheet on the analysis of north-south asymmetry in the backscattering ratios. A systematic trend along the polar orbit of discrepancy between the"true" downward proton flux and the extrapolated flux from the limited field-of-view measurements can originate from a finite z component of the proton flow velocity. Average $|V_z|$ values are less than 30 km/s in the distant plasma sheet [*Troshichev et al.*, 1999]. This is much smaller than the proton thermal speed of ~300 km/s (corresponding to a proton temperature of 500 eV) during the analyzed orbits. Therefore, the effect of proton-flux anisotropy on the north-south asymmetry in the backscattering ratio should be small. Note also that V_x is usually a dominant velocity component in the distant plasma sheet but it causes no asymmetry in the Northern and Southern Hemispheres.

4. Magnetic Shielding From the Solar Wind and Plasma Sheet Protons

The different shielding efficiencies may be attributed to difference in velocity distributions of the solar wind and plasma sheet protons. The solar wind protons have a beam-like velocity distribution with a narrow thermal spread centered at the solar wind bulk velocity in the Moon rest frame. On the other hand, the plasma sheet protons have a broad velocity distribution with a wide thermal spread. The ion thermal speed can become comparable to or larger than the bulk speed, depending on the geomagnetic conditions and Moon's location in the plasma sheet. The wide spread in velocity distributions may modify the ion dynamics around the magnetic anomalies.

We conduct four sets of test-particle simulations including only magnetic force by a dipole to investigate how the different velocity distributions of incident solar wind and plasma sheet protons ("monodirectional" and "isotropic" angular distributions combined with "monoenergy" and "Maxwellian" energy distributions) modify the magnetic shielding of the surface. We place a horizontal dipole along y axis, buried at 20 km below the surface with a surface magnetic strength of 1000 nT. The dipole field strength at 100 km above the surface is 4.6 nT, which is larger than the strongest field strength of ~2.4 nT observed at 100 km altitude [*Tsunakawa et al.*, 2010]. The lunar crustal magnetic fields actually have complex structures [e.g., *Purucker*, 2008], and these higher-order terms can enhance the shielding efficiency without increasing the field strength at 100 km altitude [*Harnett and Winglee*, 2003]. The use of a rather strong single dipole is to qualify the shielding effects by the crustal magnetic force under a simple setup of simulation. We set a simulation box with a 100 km altitude above the surface and a horizontal extent of 800×800 km^2 centered at the dipole location. We then launch a number of protons downward from the top of the box with uniformly distributed random starting locations, with a constant kinetic energy of 500 eV (monoenergy case) and Maxwell energy distributions with a characteristic energy of 500 eV (Maxwellian case), and with two different initial velocity directions: a monodirectional distribution (monodirectional case) and an isotropic distribution (isotropic case). The monodirectional case corresponds to the normal incidence of the solar wind protons to the subsolar lunar surface, whereas the isotropic case applies to any point on the lunar surface when the Moon is immersed in the isotropic plasma. We trace the particles until they strike the surface or escape from the simulation box. Figures 7a and 7b show sample proton trajectories for "monodirectional, monoenergy" and "isotropic, monoenergy" cases in the vicinity of the dipole (200 × 200 km^2). If the particles strike the surface,

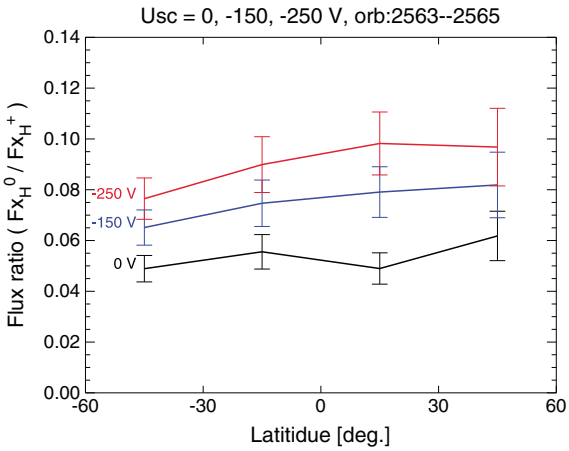

Figure 6. Backscattering ratios along the selenographic longitude of ~170°E as functions of selenographic latitude. The data are taken from ±60° latitudes divided into four ranges. Three cases for spacecraft potentials of 0, −150, −250 V are shown. Error bars represent the errors from propagation of the counting statistics of the CENA and SWIM data.

the surface locations are recorded. After we trace 4×10^6 particles, we derive a shielding efficiency for each surface bin. Here we define the shielding efficiency as $SE = 1 - N_B/N_{noB}$, where N_B is a surface density of particles landing in a particular surface bin and N_{noB} is the average surface density of particles per surface bin obtained by another simulation without the dipole field. This shielding efficiency corresponds to the one used in *Vorburger et al.*'s [2012] analysis. Positive values of the shielding efficiency indicate that the surface is shielded from the incident particles and negative values represent enhanced flux to the surface. We note that the backscattering ratio is related to the shielding efficiency as $r = r_{noB}(1 - SE)$, where r_{noB} is the backscattering ratio at the surface where no crustal field exists. The surface distributions of the calculated shielding efficiencies are shown in Figures 7c–7f.

We first look at the shielding efficiency distribution for the monodirectional, monoenergy proton case (corresponding to the "beam" solar wind protons). Figure 7c shows a large void region (SE = 1) formed mainly in the $-x$ region. This asymmetry in x direction is due to the negative B_y component above the surface, deflecting protons toward the $-x$ direction as shown in Figure 7a. We also see an enhanced-flux region ($SE < 0$) around the shielded region due to the protons that are deflected but still strike the surface. The pairs of void and enhanced-flux regions are common features of the solar wind interaction with the lunar magnetic anomalies, which can be found in the previous observations and simulations in the solar wind [*Hood and Williams*, 1989; *Wieser et al.*, 2010; *Vorburger et al.*, 2012; *Kallio et al.*, 2012].

In contrast to the large void region caused by the coherent deflection of monodirectional, monoenergy protons, Figure 7d shows different characteristics of magnetic shielding for the isotropic, monoenergy proton case. A void region (SE = 1) is formed just above the buried dipole, but its area is much smaller than that seen in the monodirectional, monoenergy proton case. We see no significant enhanced region for the isotropic, monoenergy proton case. As shown in Figure 7b, the isotropic, monoenergy protons enter the dipole field from a variety of incident angles, resulting in incoherent deflection with no favored landing locations on the surface. As a result, only the small area with strong horizontal fields is effectively shielded from the incident isotropic protons.

In addition to the angular spread, wider energy distributions also modify the magnetic shielding of the lunar surface. Figure 7 shows that the enhanced flux region ($SE < 0$) seen for the monodirectional, monoenergy case (c) is smeared out for the "monodirectional, Maxwellian" case except the magnetic cusp regions located at (0, ±25) km on the surface (e). For the Maxwellian case, the deflected lower- and higher-energy protons with both smaller and larger gyroradii strike wider regions on the surface compared to the coherently deflected monoenergy protons, resulting in the less clear boundary of the void region.

The difference of the "isotropic, Maxwellian" case (corresponding to the "broad" plasma sheet protons, Figure 7f) from the isotropic, monoenergy case (Figure 7d) is small, but we can see that some of the white bins ($SE = 1$) in Figure 7d turn into light gray ($SE < 1$) in Figure 7f. This change can be attributed to high-energy protons penetrating the dipole field. As we have seen, the combination of the angular and energy spread in proton VDFs prevents development of a large, clear void region above the buried magnetic dipole. The test particle simulations suggest that the surface is less effectively shielded by the dipole magnetic fields from the broad protons than from the beam protons, as inferred from the CENA observations in the plasma sheet and the solar wind.

We note that our model neglects any collective effects and focuses on the deflection of single particles by the magnetic force, as *Hood and Williams*'s [1989] solar wind shielding model does. The lack of collective effects hinders us from estimating the shielding efficiency quantitatively. For example, charge separation

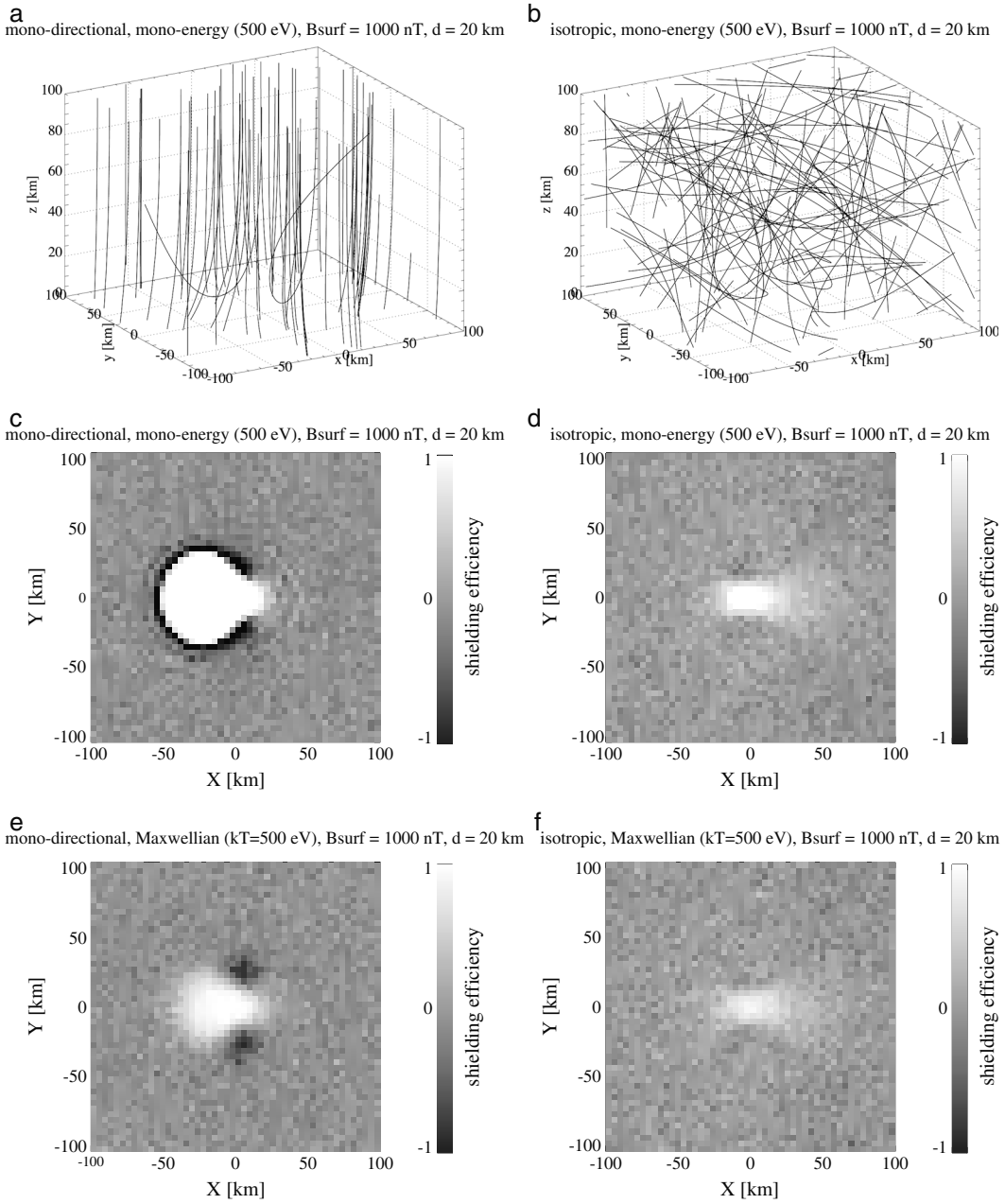

Figure 7. Test particle trajectories around a buried dipole using different proton velocity distributions. A part of proton trajectories for (a) monodirectional and (b) isotropic initial velocity distributions with a constant energy of 500 eV, in addition to the shielding efficiencies on the surface (see text for details) for (c) monodirectional and (d) isotropic monoenergy protons (500 eV) and (e) monodirectional and (f) isotropic Maxwellian protons ($kT = 500$ eV) are shown. The dipole is horizontally placed along y axis. The dipole magnetic field has $-y$ component above the surface.

electric fields will enhance the ion deflection, while plasma compression of crustal magnetic fields may result in less effective shielding because of the decrease in scale size length of the minimagnetosphere. A bow shock or shock-like formation associated with a minimagnetosphere in the solar wind might also play a role in protecting the lunar surface from the impinging protons. The different potential distributions and magnetic-field configurations above the magnetic anomalies resulting from the smaller pressure gradient and lower Mach numbers in the plasma sheet than in the solar wind will affect the upward ENA flux from the Moon as well and will be examined in future study. Nevertheless, our model can qualitatively exhibit the basic characteristics of magnetic shielding of the surface from the beam and broad ions.

5. Conclusion

We present observations of ENAs from the lunar surface in the Earth's magnetotail. The observed ENA energy spectra are fitted by the Maxwell distribution with densities of ~0.03 cm^{-3} and characteristic energies of ~100 eV. The estimated backscattering ratios of the plasma sheet protons as ENAs ~0.05–0.08 are roughly on the same order of magnitude of those of the solar wind protons ~0.1–0.2. These characteristics are similar to the backscattered ENAs in the solar wind, suggesting that the detected ENAs are plasma sheet particles backscattered as hydrogen ENAs from the lunar surface.

On the other hand, the flux ratio of the backscattered hydrogen ENAs to the downward plasma sheet protons calculated in the different selenographic latitudes exhibits no significant difference in the Northern and Southern Hemispheres. No large reduction of the backscattering ratio of plasma sheet protons is found over a large magnetic anomaly region at selenographic longitudes of ~ 170°E in the Southern Hemisphere, while the solar wind backscattering ratio drops to about the half in the Southern Hemisphere compared to that in the Northern Hemisphere. This result suggests a smaller shielding efficiency by magnetic anomalies in the plasma sheet than in the solar wind. Test-particle simulations consistently show less effective shielding in the case of broad incident ions than that in the beam-ion case. Our simulations suggest that difference between the beam-like velocity distributions of the solar wind protons and the broad velocity distributions of the plasma sheet protons may introduce different behavior of impinging protons around the magnetic anomalies. Since our model only considers magnetic forces by crustal fields, we have discussed the ion shielding effect in a mostly qualitative manner. More sophisticated models that can take into account magnetic-field deformation by plasma currents and charge separation electric fields are necessary to evaluate the shielding efficiencies quantitatively and to understand the physical processes actually working around the magnetic anomalies. It would be also important to include more realistic configurations of lunar crustal magnetic fields [*Harnett and Winglee*, 2003; *Harada et al.*, 2013]. Backscattered ENA observations within planetary magnetospheres can extend our knowledge on the solar wind interactions with solid surfaces and crustal magnetic fields to a completely different plasma regime.

Acknowledgments

The authors express their sincere thanks to the Chandrayaan-1/SARA, MAP-PACE, and MAP-LMAG team members for their great support in processing and analyzing the MAP data. The authors also express their gratitude to the system members of the SELENE and Chandrayaan-1 projects. This work was supported by a Research Fellowship for Young Scientists awarded by the Japan Society for the Promotion of Science. The Chandrayaan-1/SARA data are available in public from Indian Space Science Data Center (ISSDC). The Kaguya/MAP data are available at Kaguya Data Archive (http://l2db.selene.darts.isas.jaxa.jp/index.html.en). The Clementine 750 nm albedo data used in Figure 3 are available online at http://www.mapaplanet.com/explorer/moon.html.

Masaki Fujimoto thanks Herbert Funsten and Erika Harnett for their assistance in evaluating this paper.

References

Allegrini, F., et al. (2013), Lunar energetic neutral atom (ENA) spectra measured by the interstellar boundary explorer (IBEX), *Planet. Space Sci.*, *85*, 232–242, doi:10.1016/j.pss.2013.06.014.

Bamford, R. A., B. Kellett, W. J. Bradford, C. Norberg, A. Thornton, K. J. Gibson, I. A. Crawford, L. Silva, L. Gargaté, and R. Bingham (2012), Minimagnetospheres above the lunar surface and the formation of lunar swirls, *Phys. Rev. Lett.*, *109*, 081101, doi:10.1103/PhysRevLett.109.081101.

Barabash, S., et al. (2009), Investigation of the solar wind-Moon interaction onboard Chandrayaan-1 mission with the SARA experiment, *Curr. Sci.*, *96*(4), 526–532.

Blewett, D. T., E. I. Coman, B. R. Hawke, J. J. Gillis-Davis, M. E. Purucker, and C. G. Hughes (2011), Lunar swirls: Examining crustal magnetic anomalies and space weathering trends, *J. Geophys. Res.*, *116*, E02002, doi:10.1029/2010JE003656.

Clay, D. R., B. E. Goldstein, M. Neugebauer, and C. W. Snyder (1975), Lunar surface solar wind observations at the Apollo 12 and Apollo 15 site, *J. Geophys. Res.*, *80*, 1751–1760, doi:10.1029/JA080i013p01751.

Dyal, P., C. W. Parkin, C. W. Snyder, and D. R. Clay (1972), Measurements of lunar magnetic field interaction with the solar wind, *Nature*, *236*(5347), 381–385, doi:10.1038/236381a0.

Funsten, H. O., et al. (2013), Reflection of solar wind hydrogen from the lunar surface, *J. Geophys. Res. Planets*, *118*, 292–305, doi:10.1002/jgre.20055.

Futaana, Y., S. Barabash, M. Holmström, and A. Bhardwaj (2006), Low energy neutral atoms imaging of the Moon, *Planet. Space Sci.*, *54*(2), 132–143, doi:10.1016/j.pss.2005.10.010.

Futaana, Y., S. Barabash, M. Wieser, M. Holmström, C. Lue, P. Wurz, A. Schaufelberger, A. Bhardwaj, M. B. Dhanya, and K. Asamura (2012), Empirical energy spectra of neutralized solar wind protons from the lunar regolith, *J. Geophys. Res.*, *117*, E05005, doi:10.1029/2011JE004019.

Futaana, Y., S. Barabash, M. Wieser, C. Lue, P. Wurz, A. Vorburger, A. Bhardwaj, and K. Asamura (2013), Remote energetic neutral atom imaging of electric potential over a lunar magnetic anomaly, *Geophys. Res. Lett.*, *40*, 262–266, doi:10.1002/grl.50135.

Garrick-Bethell, I., J. W. Head, and C. M. Pieters (2011), Spectral properties, magnetic fields, and dust transport at lunar swirls, *Icarus*, *212*(2), 480–492, doi:10.1016/j.icarus.2010.11.036.

Halekas, J. S., D. A. Brain, D. L. Mitchell, R. P. Lin, and L. Harrison (2006), On the occurrence of magnetic enhancements caused by solar wind interaction with lunar crustal fields, *Geophys. Res. Lett.*, *33*, L08106, doi:10.1029/2006GL025931.

Harada, Y., et al. (2010), Interaction between terrestrial plasma sheet electrons and the lunar surface: SELENE (Kaguya) observations, *Geophys. Res. Lett.*, *37*, L19202, doi:10.1029/2010GL044574.

Harada, Y., et al. (2012), Nongyrotropic electron velocity distribution functions near the lunar surface, *J. Geophys. Res.*, *117*, A07220, doi:10.1029/2012JA017642.

Harada, Y., et al. (2013), Small-scale magnetic fields on the lunar surface inferred from plasma sheet electrons, *Geophys. Res. Lett.*, *40*, 3362–3366, doi:10.1002/grl.50662.

Harnett, E., and R. Winglee (2000), Two-dimensional MHD simulation of the solar wind interaction with magnetic field anomalies on the surface of the Moon, *J. Geophys. Res.*, *105*(A11), 24,997–25,007, doi:10.1029/2000JA000074.

Harnett, E., and R. Winglee (2002), 2.5D particle and MHD simulations of mini-magnetospheres at the Moon, *J. Geophys. Res.*, *107*(A12), 1421, doi:10.1029/2002JA009241.

Harnett, E. M., and R. M. Winglee (2003), 2.5-D fluid simulations of the solar wind interacting with multiple dipoles on the surface of the Moon, *J. Geophys. Res.*, *108*, 1088, doi:10.1029/2002JA009617.

Harnett, E. M., M. Cash, and R. M. Winglee (2013), Substorm and storm time ionospheric particle flux at the Moon while in the terrestrial magnetosphere, *Icarus*, *224*(1), 218–227, doi:10.1016/j.icarus.2013.02.022.

Hemingway, D., and I. Garrick-Bethell (2012), Magnetic field direction and lunar swirl morphology: Insights from Airy and Reiner Gamma, *J. Geophys. Res.*, *117*, E10012, doi:10.1029/2012JE004165.

Hood, L. L., and C. R. Williams (1989), The lunar swirls—Distribution and possible origins, paper presented at 19th Lunar and Planetary Science Conference, pp. 99–113, Houston, Tex., 14-18 March.

Hood, L. L., A. Zakharian, J. S. Halekas, D. L. Mitchell, R. P. Lin, M. H. Acuña, and A. B. Binder (2001), Initial mapping and interpretation of lunar crustal magnetic anomalies using Lunar Prospector magnetometer data, *J. Geophys. Res.*, *106*, 27,825–27,839, doi:10.1029/2000JE001366.

Kallio, E., et al. (2012), Kinetic simulations of finite gyroradius effects in the lunar plasma environment on global, meso, and microscales, *Planet. Space Sci.*, *74*, 146–155, doi:10.1016/j.pss.2012.09.012.

Kazama, Y., S. Barabash, M. Wieser, K. Asamura, and P. Wurz (2007), Development of an LENA instrument for planetary missions by numerical simulations, *Planet. Space Sci.*, *55*(11), 1518–1529, doi:10.1016/j.pss.2006.11.027.

Kurata, M., H. Tsunakawa, Y. Saito, H. Shibuya, M. Matsushima, and H. Shimizu (2005), Mini-magnetosphere over the Reiner Gamma magnetic anomaly region on the Moon, *Geophys. Res. Lett.*, *32*, L24205, doi:10.1029/2005GL024097.

Lin, R. P., D. L. Mitchell, D. W. Curtis, K. A. Anderson, C. W. Carlson, J. McFadden, M. H. Acuña, L. L. Hood, and A. Binder (1998), Lunar surface magnetic fields and their interaction with the solar wind: Results from Lunar Prospector, *Science*, *281*, 1480–1484, doi:10.1126/science.281.5382.1480.

Lue, C., Y. Futaana, S. Barabash, M. Wieser, M. Holmström, A. Bhardwaj, M. B. Dhanya, and P. Wurz (2011), Strong influence of lunar crustal fields on the solar wind flow, *Geophys. Res. Lett.*, *38*, L03202, doi:10.1029/2010GL046215.

Machida, S., T. Mukai, Y. Saito, M. Hirahara, T. Obara, A. Nishida, T. Terasawa, and K. Maezawa (1994), Plasma distribution functions in the Earth's magnetotail ($X_{GSM} \sim -42R_E$) at the time of a magnetospheric substorm: GEOTAIL/LEP observation, *Geophys. Res. Lett.*, *21*, 1027–1030, doi:10.1029/94GL00187.

McCann, D., S. Barabash, H. Nilsson, and A. Bhardwaj (2007), Miniature ion mass analyzer, *Planet. Space Sci.*, *55*(9), 1190–1196, doi:10.1016/j.pss.2006.11.020.

McComas, D. J., et al. (2009), Lunar backscatter and neutralization of the solar wind: First observations of neutral atoms from the Moon, *Geophys. Res. Lett.*, *36*, L12104, doi:10.1029/2009GL038794.

Mukai, T., T. Yamamoto, and S. Machida (1998), Dynamics and kinetic properties of plasmoids and flux ropes: GEOTAIL observations, in *New Perspectives on the Earth's Magnetotail, Geophys. Monogr. Ser.*, vol. 105, edited by A. Nishida, D. N. Baker, and S. W. H. Cowley, pp. 117–137, AGU, Washington, D. C., doi:10.1029/GM105p0117.

Neugebauer, M., C. W. Snyder, D. R. Clay, and B. E. Goldstein (1972), Solar wind observations on the lunar surface with the Apollo-12 ALSEP, *Planet. Space Sci.*, *20*, 1577–1591, doi:10.1016/0032-0633(72)90184-5.

Nishino, M. N., M. Fujimoto, H. Tsunakawa, M. Matsushima, H. Shibuya, H. Shimizu, F. Takahashi, Y. Saito, and S. Yokota (2012), Control of lunar external magnetic enhancements by IMF polarity: A case study, *Planet. Space Sci.*, *73*(1), 161–167, doi:10.1016/j.pss.2012.09.011.

Poppe, A. R., J. S. Halekas, G. T. Delory, and W. M. Farrell (2012), Particle-in-cell simulations of the solar wind interaction with lunar crustal magnetic anomalies: Magnetic cusp regions, *J. Geophys. Res.*, *117*, A09105, doi:10.1029/2012JA017844.

Purucker, M. E. (2008), A global model of the internal magnetic field of the Moon based on Lunar Prospector magnetometer observations, *Icarus*, *197*(1), 19–23, doi:10.1016/j.icarus.2008.03.016.

Rich, F. J., D. L. Reasoner, and W. J. Burke (1973), Plasma sheet at lunar distance: Characteristics and interactions with the lunar surface, *J. Geophys. Res.*, *78*(34), 8097–8112, doi:10.1029/JA078i034p08097.

Richmond, N. C., and L. L. Hood (2008), A preliminary global map of the vector lunar crustal magnetic field based on Lunar Prospector magnetometer data, *J. Geophys. Res.*, *113*, E02010, doi:10.1029/2007JE002933.

Richmond, N. C., L. L. Hood, J. S. Halekas, D. L. Mitchell, R. P. Lin, M. Acuña, and A. B. Binder (2003), Correlation of a strong lunar magnetic anomaly with a high-albedo region of the Descartes mountains, *Geophys. Res. Lett.*, *30*, 1395, doi:10.1029/2003GL016938.

Rodríguez, D. F., M. L. Saul, P. Wurz, S. A. Fuselier, H. O. Funsten, D. J. McComas, and E. Mobius (2012), IBEX-Lo observations of energetic neutral hydrogen atoms originating from the lunar surface, *Planet. Space Sci.*, *60*(1), 297–303, doi:10.1016/j.pss.2011.09.009.

Saito, Y., et al. (2008a), Solar wind proton reflection at the lunar surface: Low energy ion measurement by MAP-PACE onboard SELENE (KAGUYA), *Geophys. Res. Lett.*, *35*, L24205, doi:10.1029/2008GL036077.

Saito, Y., et al. (2008b), Low-energy charged particle measurement by MAP-PACE onboard SELENE, *Earth Planets Space*, *60*, 375–385.

Saito, Y., et al. (2010), In-flight performance and initial results of Plasma Energy Angle and Composition Experiment (PACE) on SELENE (Kaguya), *Space Sci. Rev.*, *154*, 265–303, doi:10.1007/s11214-010-9647-x.

Saito, Y., M. N. Nishino, M. Fujimoto, T. Yamamoto, S. Yokota, H. Tsunakawa, H. Shibuya, M. Matsushima, H. Shimizu, and F. Takahashi (2012), Simultaneous observation of the electron acceleration and ion deceleration over lunar magnetic anomalies, *Earth Planets Space*, *64*, 83–92.

Saito, Y., M. Nishino, S. Yokota, H. Tsunakawa, M. Matsushima, F. Takahashi, H. Shibuya, and H. Shimizu (2013), Night side lunar surface potential in the Earth's magnetosphere, *Adv. Space Res.*, doi:10.1016/j.asr.2013.05.011, in press.

Schaufelberger, A., P. Wurz, S. Barabash, M. Wieser, Y. Futaana, M. Holmström, A. Bhardwaj, M. B. Dhanya, R. Sridharan, and K. Asamura (2011), Scattering function for energetic neutral hydrogen atoms off the lunar surface, *Geophys. Res. Lett.*, *38*, L22202, doi:10.1029/2011GL049362.

Schubert, G., and B. R. Lichtenstein (1974), Observations of Moon-plasma interactions by orbital and surface experiment, *Rev. Geophys. Space Phys.*, *12*, 592–626, doi:10.1029/RG012i004p00592.

Shimizu, H., F. Takahashi, N. Horii, A. Matsuoka, M. Matsushima, H. Shibuya, and H. Tsunakawa (2008), Ground calibration of the high-sensitivity SELENE lunar magnetometer LMAG, *Earth Planets Space*, *60*, 353–363.

Takahashi, F., H. Shimizu, M. Matsushima, H. Shibuya, A. Matsuoka, S. Nakazawa, Y. Iijima, H. Otake, and H. Tsunakawa (2009), In-orbit calibration of the lunar magnetometer onboard SELENE (KAGUYA), *Earth Planets Space*, *61*, 1269–1274.

Troshichev, O., S. Kokubun, Y. Kamide, A. Nishida, T. Mukai, and T. Yamamoto (1999), Convection in the distant magnetotail under extremely quiet and weakly disturbed conditions, *J. Geophys. Res.*, *104*(A5), 10,249–10,263, doi:10.1029/1998JA900141.

Tsunakawa, H., H. Shibuya, F. Takahashi, H. Shimizu, M. Matsushima, A. Matsuoka, S. Nakazawa, H. Otake, and Y. Iijima (2010), Lunar magnetic field observation and initial global mapping of lunar magnetic anomalies by MAP-LMAG onboard SELENE (Kaguya), *Space Sci. Rev.*, *154*, 219–251, doi:10.1007/s11214-010-9652-0.

Tsunakawa, H., F. Takahashi, H. Shimizu, H. Shibuya, and M. Matsushima (2014), Regional mapping of the lunar magnetic anomalies at the surface: Method and its application to strong and weak magnetic anomaly regions, *Icarus*, *228*, 35–53, doi:10.1016/j.icarus.2013.09.026.

Vorburger, A., P. Wurz, S. Barabash, M. Wieser, Y. Futaana, M. Holmström, A. Bhardwaj, and K. Asamura (2012), Energetic neutral atom observations of magnetic anomalies on the lunar surface, *J. Geophys. Res.*, *117*, A07208, doi:10.1029/2012JA017553.

Vorburger, A., P. Wurz, S. Barabash, M. Wieser, Y. Futaana, C. Lue, M. Holmström, A. Bhardwaj, M. B. Dhanya, and K. Asamura (2013), Energetic neutral atom imaging of the lunar surface, *J. Geophys. Res. Space Physics*, *118*, 3937–3945, doi:10.1002/jgra.50337.

Wang, X., M. Horányi, and S. Robertson (2012), Characteristics of a plasma sheath in a magnetic dipole field: Implications to the solar wind interaction with the lunar magnetic anomalies, *J. Geophys. Res.*, *117*, A06226, doi:10.1029/2012JA017635.

Whipple, E. C. (1981), Potentials of surfaces in space, *Rep. Prog. Phys.*, *44*(11), 1197–1250, doi:10.1088/0034-4885/44/11/002.

Wieser, M., S. Barabash, Y. Futaana, M. Holmström, A. Bhardwaj, R. Sridharan, M. B. Dhanya, P. Wurz, A. Schaufelberger, and K. Asamura (2009), Extremely high reflection of solar wind protons as neutral hydrogen atoms from regolith in space, *Planet. Space Sci.*, *57*(14–15), 2132–2134, doi:10.1016/j.pss.2009.09.012.

Wieser, M., S. Barabash, Y. Futaana, M. Holmström, A. Bhardwaj, R. Sridharan, M. B. Dhanya, A. Schaufelberger, P. Wurz, and K. Asamura (2010), First observation of a mini-magnetosphere above a lunar magnetic anomaly using energetic neutral atoms, *Geophys. Res. Lett.*, *37*, L05103, doi:10.1029/2009GL041721.